Holocene Formation of Henry Ice Rise, West Antarctica, Inferred from Ice-Penetrating Radar

Martin G. Wearing [1], **Jonathan Kingslake** [1]

[1]Lamont-Doherty Earth Observatory, Columbia University, New York, USA

Key Points:

- Ice-penetrating radar data from Henry Ice Rise reveal englacial structures indicative of re-grounding and grounding-line advance.
- We present a conceptual model, constrained by data, for the formation of HIR and date formation to approximately 6 kyr before present.
- Grounding of HIR likely increased buttressing from the Ronne Ice Shelf and was a precursor to ice-sheet advance in the Weddell Sea Sector.

Corresponding author: Martin G. Wearing, `wearing@ldeo.columbia.edu`

Abstract

Ice rises are regions of grounded ice embedded within floating ice shelves. The deformation of ice past them increases the back stress generated by the ice shelf, slowing the flow of the ice sheet. We present ground-based ice-penetrating radar data from Henry Ice Rise in the Ronne Ice Shelf, West Antarctica, that indicates re-grounding during the Holocene. Relic crevasses and melt synclines are observed upstream of the present-day grounding line. We conclude that these features formed during a previous flow configuration, from which the grounding line has since advanced to its current position. In agreement with previous work, our observations can be explained if initial grounding of the ice shelf occurred on a bathymetric high, forming an ice rumple that migrated upstream and temporarily ungrounded over the topographic high. The grounding line then advanced, preserving relic basal crevasses in the newly grounded ice. Using a simple ice-flow model we simulate the burial of these crevasses. While accounting for uncertainty in accumulation, firn density, radar-derived depth, ice-thickening history, initial crevasse height and GIA, we estimate a burial time of 6 $\pm$ 2 thousand years before present for the oldest relic crevasses, indicating that the ice rise formed at approximately this time. This potentially increased the buttressing generated by the Ronne Ice Shelf, causing thickening and advance of the ice sheet. By dating the formation and providing details of ice-rise formation, these new results can provide useful constraints on both large-scale ice-sheet models and models of ice-rumple and ice-rise formation.

Plain Language Summary

We present results from an ice-penetrating radar survey on a grounded section of ice (Henry Ice Rise) within the floating Ronne Ice Shelf in West Antarctica. The radar reveals preserved crevasses at the base of the ice that are now inactive and signs of melting from contact with the ocean, both in areas that are grounded today. This implies that these areas were part of the floating ice shelf in the past. Using the distribution and size of relic crevasses within the ice, we date the formation of this grounded area to approximately 6 thousand years before present. Our date has an associated uncertainty of plus or minus 2 thousand years, primarily due to uncertainty in the rate of snowfall and the size of the crevasses when they first formed. The grounding of this area most likely allowed the West Antarctic Ice Sheet to grow to its present-day configuration.

1 Introduction

An accurate history of ice thickness and extent is important for spin-up and testing of large-scale ice-sheet models (DeConto & Pollard, 2016) and for Glacial Isostatic Adjustment (GIA) corrections to satellite measurements of ice-surface elevation change (Hanna et al., 2013). It has been assumed that the retreat of the West Antarctic Ice Sheet (WAIS) has been monotonic since the Last Glacial Maximum (LGM), 26–14 thousand years (kyr) before present (BP) (Conway et al., 1999; Bentley et al., 2014; Hillenbrand et al., 2014) and is currently at its maximum inland location. However, recent evidence suggests that the WAIS has re-advanced in the Ross and Weddell Sea sectors following a post-LGM maximum retreat (Siegert et al., 2013; Bradley et al., 2015; Kingslake et al., 2018). Other work points to a re-configuration of ice flow within the last 10 kyr in these sectors (Fahnestock et al., 2000; Hulbe & Fahnestock, 2004; Catania et al., 2005, 2006; Bingham et al., 2015; Winter et al., 2015; Kingslake et al., 2016; Brisbourne et al., 2019). Grounding-line (GL) retreat upstream of its present-day location in the Weddell Sea Sector of West Antarctica was hypothesized by Siegert et al. (2013), who used airborne ice-penetrating radar data as evidence for previous fast flow in a currently slow-flowing grounded region. Bradley et al. (2015) analysed GIA model results to show that present-day uplift rates in the Weddell Sea Sector can be best explained if the ice-sheet loading increased in the Mid- to Late- Holocene.

Further evidence for retreat upstream of the present-day GL in both the Ross and Weddell Sea Sectors of WAIS was presented by Kingslake et al. (2018). In the Ross Sea Sector, bulk radiocarbon measurements of subglacial sediments 200 km upstream of the modern GL indicate exposure to the ocean within the past 40 kyr. In the Weddell Sea Sector, ice-penetrating radar data collected over the grounded Henry Ice Rise (HIR) (Figure 1) show buried relic crevasses thought to have formed in a previous flow configuration with the GL upstream of its current position. Kingslake et al. (2018) noted that relic crevasses within HIR and surface crevassing at the downstream edge of Doake Ice Rumples (DIR) have similar spacing; 100–300 m (Figure 2). In addition, ice-sheet modelling (Kingslake et al., 2018) suggested that initial grounding of HIR resulted from GIA following post-LGM retreat. It was inferred that HIR underwent an ice-rumple configuration prior to the current ice-rise flow conditions. Due to uncertainty in model parameters and a lack of datable material in sediments, no timing constraints could be placed on GL retreat and re-advance.

Henry Ice Rise (HIR) is found within the southern section of the Ronne Ice Shelf, with the DIR to the west (Figure 1a). Ice rises and rumples are areas of grounded ice found within an ice shelf that are grounded below sea level. Ice rises are isolated flow centers with the only source of ice being local snow accumulation, whereas an ice rumple is primarily supplied by flow from an upstream ice shelf into a grounded region (Matsuoka et al., 2015). Ice rises control the large-scale flow of ice shelves (Borstad et al., 2013; Fürst et al., 2015; Wearing et al., 2015; Berger et al., 2016) and act as pinning points, generating buttressing and controlling the flow of grounded ice upstream (Goldberg et al., 2009; Favier et al., 2012; Gudmundsson, 2013; Fürst et al., 2016; Still et al., 2019). The imprint of an ice rise on ice dynamics can be seen in the surface features produced as the ice deforms past the ice rise (Fahnestock et al., 2000), with crevassing produced in areas of high deformation.

In this paper we present detailed analysis of ground-based ice-penetrating radar from HIR, first analysed by Kingslake et al. (2018), with additional profiles from the surrounding area. We extend the analysis of Kingslake et al. (2018) to conclude that relic crevasses formed as basal crevasses at former GL locations and propose a conceptual model for the formation of HIR; from initial grounding through ice-rumple flow to the formation of the ice rise, when HIR became an isolated flow center. A key development is our use of the radar data along with a simple ice-flow model to estimate the date of formation for HIR, accounting for uncertainties associated with GIA, accumulation, thickness change, and initial crevasse height.

2 Methods

2.1 Field Site: Henry Ice Rise and Doake Ice Rumples

Ice flow on HIR, constrained by satellite interferometry (Rignot et al., 2011) (MEaSUREs V2 (Rignot et al., 2017)), is predominantly away from a central divide and out into the shelf (Figure 1). The temperature of the ice-rise bed is predicted to be below the pressure-melting point (Van Liefferinge & Pattyn, 2013). Surface crevassing is visible in Radarsat backscatter imagery in most areas of the ice shelf adjacent to HIR (Jezek et al., 2013), corresponding to areas of high deformation. Crevasses form in high extensional stress areas and perpendicular to the 1st Principal Strain Axis (Figure 1c) before being advected downstream with ice flow. Further large-scale crevassing and large principal strain rates are observed as two flow units merge downstream of HIR.

At DIR the ice shelf flows on to a bathymetric high. The ice remains grounded before flowing over the northern grounding line and into the downstream ice shelf (Figure

2). At the upstream edge, the speed of the ice is reduced from approximately 70 m yr^{-1} to 40 m yr^{-1}. This is followed by acceleration to 100 m yr^{-1} across the grounded region. The acceleration is accompanied by thinning of approximately 400 m, Figure 2d. High extensional strain at the downstream edge corresponds to an area of surface crevassing, Figure 2b, with individual crevasses spaced approximately 300 m apart.

2.2 Radar Survey

The radar system used throughout this survey was the British Antarctic Survey DELORES (Deep-Looking Radar Echo Sounder) ice-penetrating radar with a 4 MHz impulse, towed behind a snowmobile at ∼15 km hr^{-1}. Data were collected during the 2013–14 and 2014–15 Antarctic summers across two survey grids on HIR, with additional individual lines on HIR and the surrounding ice shelf (Figure 1). A grid at the northern end of HIR has line spacing of 250–500 m (labelled A in Figure 1d), the other is oriented perpendicular to the ice divide on the northern peninsula of HIR, with five profiles that fully traverse the ice rise and a further five that traverse only the central section (labelled B in Figure 1d). Individual survey lines extend south to the high point of the ice-rise surface and across the southern GL. An additional survey line runs from the western edge of HIR to the eastern edge of Korff Ice Rise (KIR), approximately 230 km to the west, downstream of DIR (Figure 1 and 2b).

The radar data were processed using the software ReflexW V8.5 from Sandmeier Geophysical Research. Traces were geo-located using a dual-band global positioning system (GPS) unit mounted at the center of the radar system and sampled with regular grid spacing (2 m). Due to equipment failure, the line that connects HIR and KIR was geo-located with a single-band GPS, which provides sufficient accuracy for horizontal positions, but inaccurate vertical positions (we do not use the latter in our analysis). All traces were band-pass filtered and compiled into radargrams, which were migrated with a 2D Kirchoff algorithm, assuming a constant radar-wave velocity of 0.168 m ns^{-1}. We used the geophysical interpretation software Petrel, from Schlumberger, to map englacial structure in three dimensions. Where radar lines are closely spaced ($\leq$ 500 m separation), the subglacial topography is interpolated between lines in Petrel using Taylor series projection with a Briggs bi-harmonic smoother.

3 Results

3.1 Henry Ice Rise

The low-frequency radar survey shows reflectors corresponding to the ice base, englacial isochrones and relic crevasses. The morphology and spatial distribution of these reflectors contain information regarding the history of flow and place constraints on the migration of the GL during the formation of HIR.

3.1.1 Bed topography, isochrones and relic crevasses

The deepest bright and continuous reflector represents the ice-bed or ice-ocean interface, highlighted in blue in Figure 3. The interpolated bed topography in Figure 4 shows that the highest bed elevation is found at the northern end of the promontory at approximately 340 m below sea level. The bed deepens to the south, with the deepest areas grounded approximately 630 m below sea level.

Within parts of the northern section of HIR bordering the GL, tilted reflectors extend up from the base of the ice with smooth conformable isochrones overlying them (Figure 3a). Kingslake et al. (2018) interpreted these features as relic crevasses, indicative of a previous high-strain flow regime. The tilted reflectors all dip steeply towards the cen-

ter of HIR. They are spaced approximately 500 m apart and reach a height of 50 to 220 m above the ice-bed interface, with individual reflectors spanning up to 2 km horizontally. The spatial extent of these tilted reflectors corresponds to a transition from smooth to rough surface texture at the ice surface (Kingslake et al., 2018). Present-day surface crevassing at the HIR and DIR grounding lines has similar crevasse-lengths and spacing leading Kingslake et al. (2018) to conclude that the relic crevasses were created at previous grounding-line locations. We support this conclusion, but with the modification that our later analysis will show that the crevasses were likely to be basal crevasses, not penetrating to the surface as hypothesized by Kingslake et al. (2018).

Conformable isochrones intercept the top of the relic crevasses. Moreover, the age (and depth) of the isochrones that intercept the crevasses decreases the closer crevasses are to the present-day GL. We map conformable isochrones that cap contiguous series of relic crevasses before intersecting them (Figure 3). We refer to these layers as capping isochrones. In Figure 4, the locations of intersections between capping isochrones and relic crevasses over the northern promontory are represented as dashed curves. The southern bound of relic crevasses over the north of HIR is approximately linear and located part way up the southern slope of the topographic high (Figure 4). It is orientated approximately East-West, perpendicular to the main flow of the Ronne Ice Shelf, with increasingly younger capping isochrones intersecting relic crevasses to the north, up the topographic slope. Intersections are orientated approximately perpendicular to the main ice-shelf flow, apart from in the west, where they align with ice-shelf flow. Overall the concave-south morphology of the intersections is similar to the present-day GL.

Radar profiles that traverse the ice divide (labelled B), Figure 3, feature an area of smooth conformable isochrones beneath the ice divide approximately 18 km wide. Either side of this area, regions of tilted reflectors, also interpreted as relic crevasses, truncate progressively younger isochrones moving out towards the GL. Near the GL, isolated areas of disturbed reflectors are observed higher in the ice column, approximately 60 m below the surface (Figure 3b; East flank), adjacent to visible surface crevasses (Figure 1c). Further south on HIR conformable layers are present throughout the ice column (Figure 3c).

3.1.2 Melt synclines

Isochrone synclines (troughs) are found in close association with relic crevasses and at the southern GL (Figures 1d, 3 and 4b). Synclines are vertically aligned and increase in amplitude towards the bed. In several locations, particularly immediately upstream of relic crevasses, synclines are truncated at the bed. Synclines are interpreted as areas where there has been a persistent spatial gradient in basal melting, most likely when ice was exposed to the ocean at a GL (Catania et al., 2005, 2010). Their locations are plotted in Figures 1d, 3 and 4b.

Synclines upstream of the relic crevasses potentially mark the earliest preserved position of a former GL. Amongst the relic crevasses, within the northern promontory of HIR, synclines are traced across radar lines and, similar to the intersections of capping isochrones and relic crevasses, have similar plan-form morphology to the present-day GL. Along the lateral margins of HIR, synclines are aligned parallel to the current GL and coincide with elongated surface features (Figure 1d).

The most prominent syncline is at the southern GL, Figure 3c, with isochrones downwarped and disrupted throughout the ice column. On the ocean side of the GL, isochrones are truncated by the ice-shelf base for 11 km to the south. Unlike the northern sections of HIR, here there are no synclines where the ice is grounded, suggesting that there are no preserved relic GL positions here.

3.1.3 The absence of Raymond Arches

Raymond Arches are anticlinal structures in radar stratigraphy often found beneath or adjacent to ice divides. They form due to the non-linear rheology of ice (Raymond, 1983). Raymond Arches become visible after the ice divide has been stable for approximately one characteristic time (Martín et al., 2009); the time taken to accumulate the ice thickness in the absence of flow, for HIR, $H/a \approx 4.6$ kyr.

Unlike many ice rises (Conway et al., 1999; Martín et al., 2006; Drews et al., 2013, 2015; Kingslake et al., 2016), HIR appears to have no well-developed Raymond Arches, i.e. with arch amplitudes reaching a significant fraction of ice thickness. Within the northern promontory, some low-amplitude arches are visible, offset to the west from the present-day ice divide with the offset increasing towards the south, Figure 1d (SM Sec 2, Fig. 2 & 3). The lack of well-developed Raymond Arches, and the presence of low-amplitude arches offset from the divide, suggests an unstable and eastward migrating divide position over at least the past 5 kyr (Martín et al., 2009). Radar profiles over the southern ice divides (Western Promontory and South-East Dome) show no evidence of Raymond Arches (SM Fig. 4). There is no evidence of Raymond Arches from a previous ice-rise configuration.

3.2 Crevasses downstream of Doake Ice Rumples

The radar profile downstream of DIR (Figure 5a & b) reveals disrupted reflectors in the lower half of the ice column that extend to the ice base. Tracing flowlines downstream of DIR (Figure 2b and 5), shows that these areas with relic crevasses correspond to ice that previously flowed over DIR between 250 and 900 yr BP, where surface crevassing is visible near the GL. Conversely, the flowline originating between DIR and HIR (flowline 6), where there are no surface crevasses, intersects the radar profile in an area where the isochrones are conformable throughout the ice.

4 Interpretation

Based on the results from the ice-penetrating radar survey, we now present a conceptual model for the formation of HIR. This model is informed by the present-day configuration of steeply-dipping reflectors, isochrone synclines and the conformable isochrones, in relation to the basal topography and present-day GL. As proposed by Kingslake et al. (2018), we interpret the steeply-dipping reflectors as buried relic crevasses that formed in an area of previous high deformation. Following the conceptual model we present a framework for dating the evolution of the ice rise in Section 4.2.

4.1 Conceptual model for HIR formation

Figure 6 illustrates our conceptual model for the formation of HIR. In Stage 1, ice at the HIR completely ungrounded following the retreat of the WAIS after the LGM. This left a floating ice shelf in this location. Sometime later the ice shelf made contact with the bathymetric high at the northern end of HIR (Stage 2). Although our data do not explain the cause of re-grounding, it was most likely a result of crustal rebound due to GIA following ice unloading (Kingslake et al., 2018), which is predicted to be large in this area following the LGM (Whitehouse et al., 2012; Argus et al., 2014; Gomez et al., 2018).

The initial grounding generated resistance to the flow of the ice shelf (Stage 3). This caused compression and ice thickening upstream, leading to further grounding to the south. At the downstream GL, extensional stresses induced thinning of the ice and unground-

ing. These effects resulted in migration of the grounded area towards the south and ungrounding of the basal high (Stage 4). This is required by the distribution of paleo-GL positions, indicated by the melt synclines (Section 3.1.2) and the location of intersections between capping isochrones and relic basal crevasses (Section 3.1.1). Large basal and surface crevasses were formed at the downstream margin and were advected away with the ice flow. This configuration is seen today at DIR, with the downstream GL positioned on a southward dipping slope, suggesting that the bathymetric high beneath DIR is ungrounded (Figure 2). Favier et al. (2012) simulated ice-rumple flow in an idealized geometry, observing that the grounded area migrated off the basal high due to upstream thickening and downstream thinning. Upstream thickening and downstream thinning has also been observed about the Crary Ice Rise, Ross Ice Shelf (R. Bindschadler et al., 2005).

Following a combination of further uplift, ice thickening and dynamics in the surrounding ice shelf, the rumple began to advance in stages and re-ground towards the basal high (Stage 5). Further compression and thickening at the upstream boundary led to continued southward growth of the grounded area. As the GL advanced downstream, areas with melt synclines, basal and surface crevasses were grounded. Meanwhile extensional areas with crevasse formation advanced with the GL. The newly-grounded crevasses then deformed by vertical shear. Surface crevasses were advected further and smeared out once the GL advanced and are not clearly observable in the grounded radar profiles. The process of grounding basal crevasses was repeated as the GL advanced.

Finally, the basal high became fully grounded (Stage 6), with a history of GL advance preserved in the morphology of isochrone-crevasse intersections and melt synclines. Upstream of the disrupted isochrones and towards the center of HIR, smooth conformable layers are present, which likely formed in the compressional region upstream of the initial grounding.

4.2 Dating the evolution of Henry Ice Rise

We have developed a method that allows us to date when basal crevasses became inactive. We use this as an estimate for the advance of the GL past each location and consider the vertical displacement of individual isochrones that overlie inactive basal crevasses. In Sections 4.2.2–4.2.6 we describe the dating method, which accounts for uncertainties in the accumulation rate, GIA, ice-thickness change, vertical density profile and initial crevasse height. The latter is particularly important and uncertain. Estimating initial crevasse height requires analysis of radar data from downstream of DIR.

4.2.1 Simulating advection and burial of englacial structure downstream of DIR

We compute the depth to which crevasses formed at the downstream GL of DIR would be buried while advected with ice flow, accounting for advection, surface accumulation, strain-thinning and a range of possible initial crevasse heights. This is compared with radar observations to find a best estimate of initial crevasse height as a percentage of ice thickness.

We assume flow within the ice shelf is vertically uniform, with vertical strain rate given by the negative of the horizontal divergence $\nabla.\mathbf{u}$, assuming incompressibility. The horizontal divergence is calculated from the MEaSUREs Version 2 velocity field (Rignot et al., 2011, 2017) with Gaussian smoothing (Wearing et al., 2015; Wearing, 2016), with the ice advected from DIR to the downstream radar profile. The evolution in the thick-

ness of the ice overlying the crevasses, H_L, is given by

$$\frac{\partial H_L}{\partial t} = a - H_L \nabla . \mathbf{u}. \tag{1}$$

We assume accumulation, $a = 0.18$ m yr^{-1} (ice equivalent; see SM Sec 1). The initial thickness of the overlying ice is prescribed as a percentage of the total ice thickness at the GL of the DIR, H_0 (Fretwell et al., 2013), such that

$$H_L(t = 0) = H_0 \left(1 - \frac{\alpha_c}{100}\right), \tag{2}$$

where α_c is the percentage ice thickness occupied by the basal crevasse. The optimal initial H_L is estimated by comparing the simulated depth of crevasses to depths observed at the downstream radar profile.

Figure 5c shows the thickness of conformable ice overlying the disrupted reflectors where selected flowlines intersect the radar transect. Figure 5c & d compares the observed and simulated conformable-ice thicknesses for a range of initial crevasse heights at the DIR GL. The comparison indicates that these features form as basal crevasses rather than full-depth crevasses. The smallest root mean square (RMS) error between the simulated and observed conformable-ice thicknesses is achieved with basal crevasses that initially penetrate 40 % of the ice thickness. However, using 30% and 50% only slightly increases the RMS and for some flowlines reduces the absolute difference. Therefore, we estimate that basal crevasses penetrate approximately 40 ± 15 % of the ice thickness at the DIR GL; this encompasses the range of absolute differences and allows for extra uncertainty. Using this conservative range aims to account for the spread in results from DIR and the uncertainty associated with the assumption in the following section that conditions at DIR are similar to past conditions at HIR during ice-rumple flow.

Using observed surface strain-rates (Rignot et al., 2011, 2017; Wearing et al., 2015) with theory for linear elastic fracture mechanics (van der Veen, 1998) yields an independent estimate for basal-crevasse height of 30 % (150 m) of the ice thickness (500 m). This is near the lower bound of our empirically-estimated range (25–55 %). This may be expected because the theory assumes vertically-uniform stress, while the transition from vertical shear to vertically-uniform flow at the GL likely increases stresses as depth, extending the basal crevasses.

4.2.2 Dating grounding-line advance

We date grounding-line advance by considering the vertical displacement of individual isochrones that overlie basal crevasses. Basal crevasses form at grounding lines and we assume that they become grounded as the grounding line advances. When this occurs the crevasse transitions from a high to a low extensional stress regime and ceases to enlarge. Seawater freezes in the cavity leading to the high dielectric contrast that generates the reflections we see in radargrams. We simulate the burial of isochrones starting from an initial height equal to that when each basal crevasse became grounded. This initial height is determined from the assessment of basal crevasse height downstream of DIR, Section 4.2.1. Isochrones move downwards through the ice column according to a simple ice-flow parameterization (see below), starting at $t = -T$ when the ice first grounded, until the present day ($t = 0$). This process is iterated within the Matlab root-finding algorithm *fzero*, to find the value of T that allows the isochrone to reach its present-day depth, as observed with radar.

The ice thickness H varies over time and affects vertical motion, so must be parameterized. We also parameterize bed-uplift rate, depth-dependent density and accumulation rate, with each parameterization having an associated uncertainty. Each simulation yields a unique value of T that corresponds to a particular ice-thickness history,

accumulation rate, density profile, uplift rate and initial crevasse height. A Monte-Carlo approach is used to account for the uncertainty in these parameterizations and to compute a range of possible ages (Section 4.2.6).

4.2.3 Ice-thickness and isochrone height from radar measurements

Defining z as the vertical coordinate increasing from the ice base, we prescribe the vertical density profile (Schytt, 1958) as

$$\rho = \rho_i + (\rho_s - \rho_i) \exp\left(\frac{z-s}{L}\right), \tag{3}$$

where ρ_i is the density of ice (918 kg m^{-3}), ρ_s is the surface density (360 $\pm$ 40 kg m^{-3} (van den Broeke, 2008)), s is the surface elevation and L is the densification length scale (41.9 $\pm$ 8 m). This length scale is derived from unpublished phase-sensitive radar data collected on HIR (Kingslake & Hindmarsh, 2015), following Kingslake et al. (2016). The density profile is used to calculate the ice thickness and isochrone height from radar-derived two-way travel times (Hempel et al., 2000). Radar resolution limits the accuracy of the picked two-way travel times, so we allow the derived depths to vary in the Monte-Carlo procedure by $\pm$ 5 m (Hindmarsh et al., 2011).

4.2.4 Ice Flow

We describe horizontal isothermal ice flow with the Shallow Ice Approximation (SIA)(Hutter, 1983). This approximation is invalid at the ice divide or grounding line, but is valid in the flanks of the ice rise, where the relic crevasses have experienced most of their deformation (Raymond, 1983; Martín et al., 2006). With x representing the horizontal coordinate, the horizontal velocity is given by

$$u(x,z,t) = u_s(x,t)\left[1 - \left(1 - \frac{z}{H(t)}\right)^{n+1}\right], \tag{4}$$

where $u_s(x,t) = u(x,s,t)$ is the horizontal velocity at the surface and n is Glen's Flow Law exponent ($n = 3$). This assumes no basal sliding, consistent with a cold bed. Assuming planar flow and incompressible ice, the vertical velocity is found by differentiating this expression horizontally and integrating vertically, with the boundary condition of zero flow at the ice base, to give

$$w(z,t) = \frac{\partial u_s(t)}{\partial x}\left[\frac{H(t)}{n+2}\left(1 - \left(1 - \frac{z}{H(t)}\right)^{n+2}\right) - z\right]. \tag{5}$$

Substituting the vertical velocity at the ice surface $w_s(t) = w(H,t)$ gives

$$w(z,t) = w_s(t)\left[1 - \frac{n+2}{n+1}\left(1 - \frac{z}{H(t)}\right) + \frac{1}{n+1}\left(1 - \frac{z}{H(t)}\right)^{n+2}\right], \tag{6}$$

the Lliboutry (1979) approximation for vertical flow (see also Martín and Gudmundsson (2012)). With w_s and $H(t)$ specified (see below) we use this expression to simulate the downward motion of isochrones.

4.2.5 Ice-thickness evolution, accumulation and vertical velocity at the surface

The initial ice thickness at grounding is equal to the flotation thickness H_f. This is calculated from the present-day elevation of the ice base from radar, B (i.e., at $t =$

0), and the total GIA that has occurred since grounding, $w_{\mathrm{GIA}}T$, where w_{GIA} is the prescribed uplift rate, assumed constant in time. This gives

$$H_f = \frac{\bar{\rho}_i}{\rho_w} \left(B + w_{\mathrm{GIA}} T\right), \tag{7}$$

where $\bar{\rho}_i$ and ρ_w are the depth-averaged density of the ice and density of sea water. We account for uncertainty in w_{GIA} by considering a range of 5–13 mm yr^{-1}, covering the present-day rates from GPS measurements taken on bedrock outcrops around the Weddell Sea Sector (4–5 mm yr^{-1}) (Bradley et al., 2015), and modelled relative sea-level change for the area over the past 6 kyr ($\sim$ 12.5 mm yr^{-1}) (Gomez et al., 2018). Eustatic sea-level change is at least an order of magnitude slower than this during the period (Lambeck et al., 2014), so we consider this to be included within the uncertainty range.

Without a full mechanical model for the evolution of the ice rise after initial grounding, we simply prescribe the evolution of the ice thickness towards its present-day thickness H_0 as

$$H(t) = H_0 + (H_f - H_0) \frac{t}{T} \left(1 + \beta \left(1 - \frac{t}{T}\right)\right), \tag{8}$$

where β is an adjustable parameter between 1 and -1 that determines the thickness evolution. With $\beta = 0$, equation (8) generates a constant thickness change from H_f to H_0. For $\beta = -1$, dH/dt is initially twice the mean rate, decreasing to zero at $t = 0$. With $\beta = 1$, dH/dt is initially zero and increases through time. Equation (8) does not describe ice-flow physics, it is contrived so that a range of ice-thickness histories can be included in the Monte-Carlo procedure.

The accumulation rate a is highly uncertain. In the absence of ground measurements, the present-day accumulation rate is determined by estimates from a remote-sensing dataset, which uses the polarization of microwave emissions (Arthern et al., 2006) and a regional climate model (RACMO2.3p2; (van Wessem et al., 2018)) (see Supplementary Material (SM) Figure 1). Accumulation rates are sampled from within a 100 km radius of the radar grid. This gives a range of 0.109–0.197 m yr^{-1} ice equivalent accumulation. There may be small variations in accumulation with time; due to orographic effects as the ice rise evolved (- 4 % per 100 m elevation gain (Frieler et al., 2015)) and continent-scale changes in SMB (see SM). However, the largest uncertainty remains in the present-day accumulation rate and we choose to keep this fixed in time.

The difference between a and the time derivative of H dictates the time-varying vertical velocity at the surface,

$$w_s(t) = a - \frac{\partial H(t)}{\partial t}, \tag{9}$$

which, with (6) and (8) determines the vertical velocity profile.

4.2.6 Monte-Carlo procedure

As described above, each combination of parameters (accumulation rate, ice-thickness change, density, GIA and initial crevasse height) provides a different estimate of the date at which a crevasse became inactive, T. The impact of uncertainties associated with each parameter is explored by performing 20,000 simulations, each with parameters chosen randomly from a uniform distribution, with ranges summarized in Table 1. Assuming each parameter combination is equally likely, the results for T provide a probability distribution for the date when crevasses became inactive in each location. After 20,000 simulations the mean age and standard deviation converge to within 50 and 30 years respectively, i.e. additional simulations change the distribution of T only slightly (see SM Figure 9).

In some locations close to the present-day GL, relic-crevasse height exceeds the lower bound on initial crevasse height ($0.25H_f$). Therefore, some simulations do not provide an estimate of T and are ignored. These relic crevasses are located far from the oldest relic crevasses and ignoring them does not affect estimates of timing of initial grounding.

4.3 Timing of ice-rise evolution

Comparing ice-surface features downstream of grounded areas, such as flow stripes and crevasses, with the present-day flow allows estimation of the time since grounding (Fahnestock et al., 2000; Hulbe & Fahnestock, 2004; Siegert et al., 2013). This is limited by the residence time of the ice within the ice shelf. Surface features downstream of HIR consistent with the presence of an ice rise extend to the ice-shelf edge, suggesting that HIR has been present for at least the residence time of ice near HIR, approximately 1 kyr, assuming constant ice-shelf velocity.

To further constrain the date of grounding, we apply the method described in Section 4.2. We use the results for the heights of basal crevasses downstream of DIR as indicative of the typical height of basal crevasses formed at ice-rumple and ice-rise GLs, 40 ± 15 % of ice thickness. To date advance from the earliest preserved ice-rumple configuration, we use the height of relic crevasses, bed elevation and ice thickness at the upstream bound of relic crevassing (SM; Figures 2 & 7). An example of how the dating method is applied is given in the SM Section 3 for radar line B.

In several locations, particularly along the eastern flank of HIR, isochrones are downwarped by complex flow caused by concentrated melt, forming melt synclines. Our model assumes simple SIA-flow, so we disregard age estimates from these locations. The mean for the initial advance of the GL on the western flank using lines unaffected by concentrated melt is 5.9 kyr (Figure 7), with a combined standard deviation (Rudmin, 2010) (σ) of 2.1 kyr. In general, age estimates decrease towards the GL, with relic crevasses at the edges of the radar lines on the western flank becoming inactive approximately 3 kyr BP (SM; Figure 2).

Across the northern promontory, dating the earliest relic crevasses that are unaffected by melt yields a mean age of 3.3 kyr ($\sigma = 1.6$ kyr). This provides one estimate of the age of initial GL advance over the northern promontory, but this may be an underestimate because the earliest (furthest upstream) relic crevasses often coincide with melt synclines (Figure 7 in SM) and are therefore discarded from the analysis. Moving out towards the GL, age estimates generally decrease, which is consistent with GL advance towards its current location, with the most downstream relic crevasses surveyed grounding approximately 1 kyr BP.

At the southern GL, the absence of synclines from previous GL positions suggests that southwards GL migration may have occurred continuously. The deep bathymetry to the south (Fretwell et al., 2013) and ocean melting likely prevented further migration upstream. Using estimated melt rates of between 1 m yr^{-1} ((Joughin, 2003; Timmermann & Goeller, 2017)) and 3.5 m yr^{-1} (using the minimum $\nabla.\mathbf{u}$ on the ocean side of the GL; $-4{\times}10^{-3}$ yr^{-1} (Wearing, 2016), in the steady-state continuity equation) suggests that the GL has been here for at least 260 - 900 yrs given the current ice thickness (900 m), but we cannot rule out it being here for much longer.

In summary, from the residence time of ice within the shelf, grounding must have occurred at least 1 kyr ago. Estimates dating the earliest relic basal crevasses on the western flank suggests an age of approximately 5.9 kyr ($\pm$ 2.1 kyr). Advance over the north-

ern promontory occurred at least 3.3 kyr (± 1.6 kyr) ago. These dates provide ages for the transition from ice rumple towards ice rise, but initial grounding would have occurred sometime before this. There may have been a period of stability before advance allowing the formation of melt synclines upstream of the earliest preserved basal crevasses.

This estimated age (5.9 ± 2.1 kyr) is potentially greater than the characteristic time for the ice rise, suggesting that if flow had been stable over this time, we should expect to see Raymond Arches. However, our analysis demonstrates that the ice rise continued to evolve, with further grounding in all directions, with newly-grounded areas forming in the past 1 kyr. This continued evolution could have suppressed Raymond-arch growth and led to the offset between the ice divide and the under-developed arches on the northern promontory.

5 Discussion

Here we discuss an alternative hypothesis that can explain some of the englacial structures discussed above, the implications for large-scale dynamics of this sector of WAIS, uncertainties associated with the dating methodology and the outlook for future work.

5.1 Alternative Hypothesis

Our conceptual model describes a formation scenario for HIR with complete ungrounding following post-LGM retreat and then subsequent re-grounding. It is also possible for ice rises to form at the periphery of an ice sheet as the ice-sheet GL retreats through the area, leaving the ice rise as an isolated grounded region (Matsuoka et al., 2015). This process has been captured in idealized model simulations by Favier and Pattyn (2015). In the case of HIR, this alternative formation scenario is permissible if the retreat of the ice-sheet GL also resulted in the GL surrounding HIR retreating then re-advancing. However, simulations (Favier & Pattyn, 2015) suggest it is likely that this smaller ice rise would remain grounded over the topographic high. We observe relic crevassing and melt synclines upstream of the topographic high, suggesting that ice was ungrounded here and underwent a period of ice-rumple flow prior to full re-grounding. This argument is further strengthened by the lack of Raymond Arches from a smaller and older ice rise. Further numerical modelling of the two alternative formation scenarios could help determine how ice rumples and ice rises form, flow and evolve relative to basal topography.

5.2 Implications of timing for large-scale changes

The formation and growth of HIR is expected to significantly increase the buttressing generated by the Ronne Ice Shelf, leading to thickening and advance of the main ice sheet (Goldberg et al., 2009; Favier et al., 2012; Kingslake et al., 2018). Simulations from Kingslake et al. (2018) rely on grounding over the ice rises in the Weddell and Ross Sea sectors to re-advance the GL to its current location. This provides a mechanism for the re-advance invoked by Bradley et al. (2015). These processes may be particularly important for the WAIS, where mantle viscosity is relatively low and GIA can respond on relatively short time- and length- scales (Gomez et al., 2018; Barletta et al., 2018).

The transition from fast to slow flow over the Bungenstock Ice Rise (BIR) is thought to have occurred up to 4 kyr BP (Siegert et al., 2013). We estimate that the transition at HIR from rumple-flow to the present-day ice-rise scenario occurred, approximately 6 ± 2 kyr BP. Grounding and the consequent increase in buttressing may have occurred at or before this time. This suggests that the grounding of HIR may have been a precursor to changing dynamics at BIR. With HIR positioned immediately to the north of BIR, it is reasonable to speculate that the grounding of HIR may have caused the stagnation of BIR.

5.3 Dating uncertainties

Uncertainty in the dates derived above arise from the combined uncertainties in accumulation rate, ice-thickness change, radar depth-measurements, vertical density, GIA and initial crevasse height. Each panel in Figure 8 displays the frequency distribution of age estimates obtained from 20,000 Monte-Carlo runs, for the earliest relic crevasse on radar line A_1 - A_2, when uncertainties in each parameter are considered separately. The largest contributors to dating uncertainty are the accumulation rate (Figure 8b) and the initial crevasse depth (Figure 8f). When all uncertainties are included (Figure 8a) the estimates are approximately normally distributed. In contrast, when only uncertainty in the initial crevasse height is included (Figure 8f), the modal frequency is near the upper bound of the distribution. This can be explained by considering the decreasing vertical velocity experienced by an isochrone as it moves down through the ice (equation (6)). Taller crevasses are initially advected downwards relatively quickly, and slow as they get deeper. Therefore, crevasses that were initially tall (40–55% of the ice thickness) have an increased concentration of ages near the upper end of the distribution. In contrast, short crevasses (25–40%) are initially buried more slowly and variations in the height lead to a larger spread in ages at the lower end of the distribution.

We estimated a range of initial crevasse heights (25–55%) using radar data from downstream of DIR. A major limitation of our approach arises from the assumption that relic crevasses on HIR formed in a similar manner to those at DIR. Relic crevasses along the East and West flanks of HIR likely formed in shear rather than extensional stress and the dynamics of the Ronne Ice Shelf were likely very different in the mid-Holocene than today. Therefore, basal crevasses may have formed in a different stress regime. Due to this limitation we used a large range of initial crevasse depths, which significantly increase dating uncertainty. With additional radar profiles downstream of DIR and HIR or model simulations of crevasse formation in relevant stress regimes, future work may be able to better constrain initial basal-crevasse height and, therefore, the dates when the crevasses became inactive.

The other main contributor to dating uncertainty is accumulation rate. A large range in present-day accumulation rate arises from the mismatch between accumulation estimates from remote sensing (Arthern et al., 2006) and regional climate modelling (van Wessem et al., 2018). In addition, accumulation rates may have changed in time. Over the last 6 kyr accummulation at the WAIS divide was $\sim$10 % higher than present day (Koutnik et al., 2016). If accumulation at HIR scales with past variations at WAIS divide, our age estimates must be reduced by approximately 10 % (see SM Section 6). Improved estimates of accumulation from shallow radar surveys, an ice core on HIR, or high-resolution climate modelling could reduce this uncertainty.

Basal melting could also affect our dating estimates. At locations where spatially-varying melting is evident (from isochrone synclines) we have omitted date estimates. However, uniform melting of the ice base, which we cannot rule out, would lead us to overestimate the age of relic crevasses. However, we expect melting to be negligible after the ice is grounded, in comparison to the spatially-focused melting expected at GLs.

5.4 Outlook

As detailed in our new conceptual model of the formation of HIR, constrained by radar-observed englacial structure, age estimates correspond to when crevasses became inactive and preserved in the slow-moving HIR. This occurred during the transition from an ice-rumple to an ice rise. Initial grounding on the topographic high beneath HIR occurring some time before this. One way to confirm re-grounding and potentially improve our dating would be to drill to the base of HIR, analysing the age and properties of the

ice recovered and to collect basal sediment to date the last exposure to a marine environment, as has been done previously on the Ross Ice Shelf tributary ice streams (Kingslake et al., 2018).

This work highlights the complexity of ice-shelf pinning over bathymetric high points. Continent-scale ice-sheet models currently cannot capture the detailed dynamics of pinning-point formation, as they lack sufficient spatial resolution. Regional, high-resolution ice-flow modelling could test our conceptual model of HIR formation and produce features observed in the radar survey, such as relic basal crevasses and synclines, to better constrain the timing of this process. Future geophysics campaigns could seek englacial features in ice rises in the Ross Ice Sea similar to those observed in HIR for dating constraints and mechanistic explanations for the re-advance of the GL here, as reported by Kingslake et al. (2018) and to build on the work of Fahnestock et al. (2000); Catania et al. (2006); Hulbe et al. (2013) in conjunction with estimates of GL retreat through the sector (Conway et al., 1999; Martín et al., 2006).

Future work should aim to place the re-grounding of HIR in context with other Holocene changes in this sector, such as the transition at Korff Ice Rise, from North-South flow to stable ice-divide flow prior to 2.5 kyr BP (Kingslake et al., 2016; Brisbourne et al., 2019), the potential retreat of WAIS GL inland of its current position (Siegert et al., 2013; Bradley et al., 2015; Kingslake et al., 2018) and other flow switching in the Institute and Möller ice stream system (Bingham et al., 2015; Winter et al., 2015). There is also no current dating constraint on the formation and evolution of DIR, which may be significant for controlling the GL position of ice rises and the main ice sheet. We will require a deeper understanding of the formation and evolution of ice rumples before such constraints can be obtained.

6 Conclusion

Using a combination of modelling and radar data, we propose the most detailed conceptual model to-date for the formation of an ice rise through ice-shelf grounding. At Henry Ice Rise, West Antarctica, we date the transition from ice rumple to ice rise to 5.9 $\pm$ 2.1 kyr BP, which potentially pre-dates flow reorganizations upstream (Siegert et al., 2013; Bradley et al., 2015) and at neighbouring Korff Ice Rise (Kingslake et al., 2016). These are the first constraints on the timing of flow changes in this location and is the first time, to our knowledge, that burial of basal crevasses has been exploited to date ice-flow changes (although Conway et al. (2002) used buried surface crevasses to date ice-stream stagnation, and Siegert et al. (2013) dated stagnation of an ice rise using disrupted deep layers). Our conceptual model can inform, and be improved by, detailed modelling of ice-rise formation, and could be tested with a combination of new geophysics, and ice-core and subglacial sediment analysis. The new timing constraint can be used to tune ice-sheet models (e.g., Albrecht et al. (2019), and our new dating method can be applied to other ice rises formed through re-grounding (R. A. Bindschadler et al., 1990). This work further demonstrates the complexity of ice-rise/ice-rumple dynamics (e.g., Matsuoka et al. (2015)), and highlights their importance for past and future ice-sheet change.

Parameter	Range
GIA	5 - 13 mm yr^{-1}
Ice-thickness change	As determined by eqn (8) with -1 $\leq$ β $\leq$ 1
Accumulation rate	0.109 - 0.197 m yr^{-1}
Bed depth	variable (radar measurement) $\pm$ 5 m
Layer depth	variable (radar measurement) $\pm$ 5 m
Surface elevation	variable (dual-band GPS) $\pm$ 1 m
Surface density	320 - 400 kg m^{-3}
Vertical densification scale	33.9 - 49.9 m
Basal crevasse height	25 - 55 % of flotation thickness

Table 1. All uncertainties used in the Monte-Carlo simulation to calculate the age of buried crevasses. In the Monte-Carlo procedure the value of each parameter is uniformly distribution within this range.

Acknowledgments

Ice-penetrating radar data can be obtained from the UK Polar Data Centre at http://doi.org/99d.

The fieldwork was funded by Natural Environmental Research Council grant NE/J008087/1, led by Richard Hindmarsh, British Antarctic Survey. Logistical support was provided by many members of the British Antarctic Survey's air unit and field operations team. Thank you particularly to Iain Rudkin and Scott Webster for their assistance in the field.

References

Albrecht, T., Winkelmann, R., & Levermann, A. (2019, may). Glacial cycles simulation of the Antarctic Ice Sheet with PISM – Part 1: Boundary conditions and climatic forcing. *The Cryosphere Discussions*(April), 1–56. Retrieved from `https://www.the-cryosphere-discuss.net/tc-2019-71/` doi: 10.5194/tc-2019-71

Argus, D. F., Peltier, W. R., Drummond, R., & Moore, A. W. (2014, jul). The Antarctica component of postglacial rebound model ICE-6G_C (VM5a) based on GPS positioning, exposure age dating of ice thicknesses, and relative sea level histories. *Geophysical Journal International*, *198*(1), 537–563. Retrieved from `http://academic.oup.com/gji/article/198/1/537/2874192/The-Antarctica-component-of-postglacial-rebound` doi: 10.1093/gji/ggu140

Arthern, R. J., Winebrenner, D. P., & Vaughan, D. G. (2006). Antarctic snow accumulation mapped using polarization of 4.3-cm wavelength microwave emission. *Journal of Geophysical Research*, *111*(D6), D06107. Retrieved from `http://doi.wiley.com/10.1029/2004JD005667` doi: 10.1029/2004JD005667

Barletta, V. R., Bevis, M., Smith, B. E., Wilson, T., Brown, A., Bordoni, A., ... Wiens, D. A. (2018, jun). Observed rapid bedrock uplift in Amundsen Sea Embayment promotes ice-sheet stability. *Science*, *360*(6395), 1335–1339. Retrieved from `http://www.sciencemag.org/lookup/doi/10.1126/science.aao1447` doi: 10.1126/science.aao1447

Bentley, M. J., Ó Cofaigh, C., Anderson, J. B., Conway, H., Davies, B., Graham, A. G., ... Zwartz, D. (2014, sep). A community-based geological reconstruction of Antarctic Ice Sheet deglaciation since the Last Glacial Maximum. *Quaternary Science Reviews*, *100*, 1–9. Retrieved from

https://linkinghub.elsevier.com/retrieve/pii/S0277379114002546 doi: 10.1016/j.quascirev.2014.06.025

Berger, S., Favier, L., Drews, R., Derwael, J.-J., & Pattyn, F. (2016, feb). The control of an uncharted pinning point on the flow of an Antarctic ice shelf. *Journal of Glaciology*, *62*(231), 37–45. Retrieved from https://www.cambridge.org/core/product/identifier/S0022143016000071/type/journal{_}article doi: 10.1017/jog.2016.7

Bindschadler, R., Vornberger, P., & Gray, L. (2005, sep). Changes in the ice plain of Whillans Ice Stream, West Antarctica. *Journal of Glaciology*, *51*(175), 620–636. Retrieved from https://www.cambridge.org/core/product/identifier/S0022143000210824/type/journal{_}article doi: 10.3189/172756505781829070

Bindschadler, R. A., Roberts, E. P., & Iken, A. (1990, jan). Age of Crary Ice Rise, Antarctica, Determined from Temperature-Depth Profiles. *Annals of Glaciology*, *14*(1970), 13–16. Retrieved from https://www.cambridge.org/core/product/identifier/S0260305500008168/type/journal{_}article doi: 10.3189/S0260305500008168

Bingham, R. G., Rippin, D. M., Karlsson, N. B., Corr, H. F. J., Ferraccioli, F., Jordan, T. A., ... Siegert, M. J. (2015, apr). Ice-flow structure and ice dynamic changes in the Weddell Sea sector of West Antarctica from radar-imaged internal layering. *Journal of Geophysical Research: Earth Surface*, *120*(4), 655–670. Retrieved from http://doi.wiley.com/10.1002/2014JF003291 doi: 10.1002/2014JF003291

Borstad, C. P., Rignot, E., Mouginot, J., & Schodlok, M. P. (2013, dec). Creep deformation and buttressing capacity of damaged ice shelves: theory and application to Larsen C ice shelf. *The Cryosphere*, *7*(6), 1931–1947. Retrieved from http://www.the-cryosphere.net/7/1931/2013/https://www.the-cryosphere.net/7/1931/2013/ doi: 10.5194/tc-7-1931-2013

Bradley, S. L., Hindmarsh, R. C., Whitehouse, P. L., Bentley, M. J., & King, M. A. (2015, mar). Low post-glacial rebound rates in the Weddell Sea due to Late Holocene ice-sheet readvance. *Earth and Planetary Science Letters*, *413*, 79–89. Retrieved from http://dx.doi.org/10.1016/j.epsl.2014.12.039https://linkinghub.elsevier.com/retrieve/pii/S0012821X14008000 doi: 10.1016/j.epsl.2014.12.039

Brisbourne, A. M., Martín, C., Smith, A. M., Baird, A. F., Kendall, J. M., & Kingslake, J. (2019, jan). Constraining Recent Ice Flow History at Korff Ice Rise, West Antarctica, Using Radar and Seismic Measurements of Ice Fabric. *Journal of Geophysical Research: Earth Surface*, *124*(1), 175–194. Retrieved from http://doi.wiley.com/10.1029/2018JF004776 doi: 10.1029/2018JF004776

Catania, G. A., Conway, H., Raymond, C., & Scambos, T. (2005, sep). Surface morphology and internal layer stratigraphy in the downstream end of Kamb Ice Stream, West Antarctica. *Journal of Glaciology*, *51*(174), 423–431. Retrieved from https://www.cambridge.org/core/product/identifier/S0022143000209490/type/journal{_}article doi: 10.3189/172756505781829142

Catania, G. A., Conway, H., Raymond, C. F., & Scambos, T. A. (2006). Evidence for floatation or near floatation in the mouth of Kamb Ice Stream, West Antarctica, prior to stagnation. *Journal of Geophysical Research*, *111*(F1), F01005. Retrieved from http://doi.wiley.com/10.1029/2005JF000355 doi: 10.1029/2005JF000355

Catania, G. A., Hulbe, C., & Conway, H. (2010, sep). Grounding-line basal melt rates determined using radar-derived internal stratigraphy. *Journal of Glaciology*, *56*(197), 545–554. Retrieved from https://www.cambridge.org/core/product/identifier/S0022143000207168/type/journal{_}article doi:

10.3189/002214310792447842

Conway, H., Catania, G., Raymond, C. F., Gades, A. M., Scambos, T. A., & Engelhardt, H. (2002, oct). Switch of flow direction in an Antarctic ice stream. *Nature*, *419*(6906), 465–467. Retrieved from http://www.nature.com/articles/nature01081 doi: 10.1038/nature01081

Conway, H., Hall, B. L., Denton, G. H., Gades, A. M., & Waddington, E. D. (1999, oct). Past and Future Grounding-Line Retreat of the West Antarctic Ice Sheet. *Science*, *286*(5438), 280–283. Retrieved from http://www.sciencemag.org/cgi/doi/10.1126/science.286.5438.280 doi: 10.1126/science.286.5438.280

DeConto, R. M., & Pollard, D. (2016, mar). Contribution of Antarctica to past and future sea-level rise. *Nature*, *531*(7596), 591–597. Retrieved from http://dx.doi.org/10.1038/nature17145http://www.nature.com/articles/nature17145 doi: 10.1038/nature17145

Depoorter, M. A., Bamber, J. L., Griggs, J. A., Lenaerts, J. T. M., Ligtenberg, S. R. M., van den Broeke, M. R., & Moholdt, G. (2013, oct). Calving fluxes and basal melt rates of Antarctic ice shelves. *Nature*, *502*(7469), 89–92. Retrieved from http://dx.doi.org/10.1038/nature12567http://www.nature.com/articles/nature12567 doi: 10.1038/nature12567

Drews, R., Martín, C., Steinhage, D., & Eisen, O. (2013, jul). Characterizing the glaciological conditions at Halvfarryggen ice dome, Dronning Maud Land, Antarctica. *Journal of Glaciology*, *59*(213), 9–20. Retrieved from https://www.cambridge.org/core/product/identifier/S0022143000203365/type/journal{_}article doi: 10.3189/2013JoG12J134

Drews, R., Matsuoka, K., Martín, C., Callens, D., Bergeot, N., & Pattyn, F. (2015, mar). Evolution of Derwael Ice Rise in Dronning Maud Land, Antarctica, over the last millennia. *Journal of Geophysical Research: Earth Surface*, *120*(3), 564–579. Retrieved from http://doi.wiley.com/10.1002/2014JF003246 doi: 10.1002/2014JF003246

Fahnestock, M. A., Scambos, T. A., Bindschadler, R. A., & Kvaran, G. (2000, sep). A millennium of variable ice flow recorded by the Ross Ice Shelf, Antarctica. *Journal of Glaciology*, *46*(155), 652–664. Retrieved from https://www.cambridge.org/core/product/identifier/S0022143000212677/type/journal{_}article doi: 10.3189/172756500781832693

Favier, L., Gagliardini, O., Durand, G., & Zwinger, T. (2012, jan). A three-dimensional full Stokes model of the grounding line dynamics: effect of a pinning point beneath the ice shelf. *The Cryosphere*, *6*(1), 101–112. Retrieved from https://www.the-cryosphere.net/6/101/2012/ doi: 10.5194/tc-6-101-2012

Favier, L., & Pattyn, F. (2015, jun). Antarctic ice rise formation, evolution, and stability. *Geophysical Research Letters*, *42*(11), 4456–4463. Retrieved from http://doi.wiley.com/10.1002/2015GL064195 doi: 10.1002/2015GL064195

Fretwell, P., Pritchard, H. D., Vaughan, D. G., Bamber, J. L., Barrand, N. E., Bell, R., ... Zirizzotti, A. (2013, feb). Bedmap2: improved ice bed, surface and thickness datasets for Antarctica. *The Cryosphere*, *7*(1), 375–393. Retrieved from https://www.the-cryosphere.net/7/375/2013/ doi: 10.5194/tc-7-375-2013

Frieler, K., Clark, P. U., He, F., Buizert, C., Reese, R., Ligtenberg, S. R., ... Levermann, A. (2015). Consistent evidence of increasing Antarctic accumulation with warming. *Nature Climate Change*, *5*(4), 348–352. doi: 10.1038/nclimate2574

Fürst, J. J., Durand, G., Gillet-Chaulet, F., Merino, N., Tavard, L., Mouginot, J., ... Gagliardini, O. (2015, aug). Assimilation of Antarctic velocity observations provides evidence for uncharted pinning points. *The Cryosphere*, *9*(4), 1427–

738 1443. Retrieved from https://www.the-cryosphere.net/9/1427/2015/ doi:
739 10.5194/tc-9-1427-2015
740 Fürst, J. J., Durand, G., Gillet-Chaulet, F., Tavard, L., Rankl, M., Braun, M., &
741 Gagliardini, O. (2016, may). The safety band of Antarctic ice shelves. *Nature*
742 *Climate Change*, *6*(5), 479–482. Retrieved from http://www.nature.com/
743 articles/nclimate2912 doi: 10.1038/nclimate2912
744 Goldberg, D., Holland, D. M., & Schoof, C. (2009, dec). Grounding line move-
745 ment and ice shelf buttressing in marine ice sheets. *Journal of Geophysical Re-*
746 *search*, *114*(F4), F04026. Retrieved from http://doi.wiley.com/10.1029/
747 2008JF001227 doi: 10.1029/2008JF001227
748 Gomez, N., Latychev, K., & Pollard, D. (2018, may). A Coupled Ice Sheet–Sea Level
749 Model Incorporating 3D Earth Structure: Variations in Antarctica during the
750 Last Deglacial Retreat. *Journal of Climate*, *31*(10), 4041–4054. Retrieved
751 from http://journals.ametsoc.org/doi/10.1175/JCLI-D-17-0352.1 doi:
752 10.1175/JCLI-D-17-0352.1
753 Gudmundsson, G. H. (2013, apr). Ice-shelf buttressing and the stability of ma-
754 rine ice sheets. *The Cryosphere*, *7*(2), 647–655. Retrieved from http://
755 www.the-cryosphere.net/7/647/2013/https://www.the-cryosphere.net/
756 7/647/2013/ doi: 10.5194/tc-7-647-2013
757 Hanna, E., Navarro, F. J., Pattyn, F., Domingues, C. M., Fettweis, X., Ivins,
758 E. R., ... Zwally, H. J. (2013, jun). Ice-sheet mass balance and climate
759 change. *Nature*, *498*(7452), 51–59. Retrieved from http://dx.doi.org/
760 10.1038/nature12238http://www.nature.com/articles/nature12238 doi:
761 10.1038/nature12238
762 Haran, T., Bohlander, J., Scambos, T., Painter, T., & Fahnestock, M. (2005).
763 *MODIS Mosaic of Antarctica 2003-2004 (MOA2004) Image Map.* Retrieved
764 from http://dx.doi.org/10.7265/N5ZK5DM5 doi: 10.7265/N5ZK5DM5
765 Hempel, L., Thyssen, F., Gundestrup, N., Clausen, H. B., & Miller, H. (2000,
766 sep). A comparison of radio-echo sounding data and electrical con-
767 ductivity of the GRIP ice core. *Journal of Glaciology*, *46*(154), 369–
768 374. Retrieved from https://www.cambridge.org/core/product/
769 identifier/S0022143000212781/type/journal{_}article doi:
770 10.3189/172756500781833070
771 Hillenbrand, C.-D., Bentley, M. J., Stolldorf, T. D., Hein, A. S., Kuhn, G., Graham,
772 A. G., ... Sugden, D. E. (2014, sep). Reconstruction of changes in the Weddell
773 Sea sector of the Antarctic Ice Sheet since the Last Glacial Maximum. *Qua-*
774 *ternary Science Reviews*, *100*, 111–136. Retrieved from http://dx.doi.org/
775 10.1016/j.quascirev.2013.07.020https://linkinghub.elsevier.com/
776 retrieve/pii/S0277379113002850 doi: 10.1016/j.quascirev.2013.07.020
777 Hindmarsh, R. C. A., King, E. C., Mulvaney, R., Corr, H. F. J., Hiess, G., &
778 Gillet-Chaulet, F. (2011, jun). Flow at ice-divide triple junctions: 2.
779 Three-dimensional views of isochrone architecture from ice-penetrating
780 radar surveys. *Journal of Geophysical Research: Earth Surface*, *116*(F2),
781 1–14. Retrieved from http://doi.wiley.com/10.1029/2009JF001622 doi:
782 10.1029/2009JF001622
783 Hulbe, C. L., & Fahnestock, M. A. (2004, sep). West Antarctic ice-stream dis-
784 charge variability: mechanism, controls and pattern of grounding-line re-
785 treat. *Journal of Glaciology*, *50*(171), 471–484. Retrieved from https://
786 www.cambridge.org/core/product/identifier/S0022143000215256/type/
787 journal{_}article doi: 10.3189/172756504781829738
788 Hulbe, C. L., Scambos, T. a., Lee, C.-K., Bohlander, J., & Haran, T. (2013,
789 aug). Recent changes in the flow of the Ross Ice Shelf, West Antarc-
790 tica. *Earth and Planetary Science Letters*, *376*, 54–62. Retrieved from
791 https://linkinghub.elsevier.com/retrieve/pii/S0012821X13003294
792 doi: 10.1016/j.epsl.2013.06.013

Hutter, K. (1983). The Application of the Shallow-Ice Approximation. In *Theoretical glaciology* (pp. 256–332). Dordrecht: Springer Netherlands. Retrieved from http://www.springerlink.com/index/10.1007/978-94-015-1167-4{_}5 doi: 10.1007/978-94-015-1167-4_5

Jezek, K. C., Curlander, J. C., Carsey, F., Wales, C., & Barry, R. G. (2013). *RAMP AMM-1 SAR Image Mosaic of Antarctica, Version 2.* Boulder, Colorado USA. NSIDC: National Snow and Ice Data Center. doi: 10.5067/8AF4ZRPULS4H

Joughin, I. (2003). Melting and freezing beneath Filchner-Ronne Ice Shelf, Antarctica. *Geophysical Research Letters*, *30*(9), 1477. Retrieved from http://doi.wiley.com/10.1029/2003GL016941 doi: 10.1029/2003GL016941

Kingslake, J., & Hindmarsh, R. C. (2015). *Phase-sensitive radar measurements near ice divides on ice rises in the Ronne Ice Shelf region.* Retrieved from https://data.bas.ac.uk/full-record.php?id=GB/NERC/BAS/PDC/00844 doi: 10.5285/f27e42e6-8abf-4970-81c8-270529f8295f

Kingslake, J., Martín, C., Arthern, R. J., Corr, H. F. J., & King, E. C. (2016, sep). Ice-flow reorganization in West Antarctica 2.5 kyr ago dated using radar-derived englacial flow velocities. *Geophysical Research Letters*, *43*(17), 9103–9112. Retrieved from http://doi.wiley.com/10.1002/2016GL070278 doi: 10.1002/2016GL070278

Kingslake, J., Scherer, R. P., Albrecht, T., Coenen, J., Powell, R. D., Reese, R., ... Whitehouse, P. L. (2018, jun). Extensive retreat and re-advance of the West Antarctic Ice Sheet during the Holocene. *Nature*, *558*(7710), 430–434. Retrieved from http://dx.doi.org/10.1038/s41586-018-0208-xhttp://www.nature.com/articles/s41586-018-0208-x doi: 10.1038/s41586-018-0208-x

Koutnik, M. R., Fudge, T. J., Conway, H., Waddington, E. D., Neumann, T. A., Cuffey, K. M., ... Taylor, K. C. (2016, may). Holocene accumulation and ice flow near the West Antarctic Ice Sheet Divide ice core site. *Journal of Geophysical Research: Earth Surface*, *121*(5), 907–924. Retrieved from http://doi.wiley.com/10.1002/2015JF003668 doi: 10.1002/2015JF003668

Lambeck, K., Rouby, H., Purcell, A., Sun, Y., & Sambridge, M. (2014, oct). Sea level and global ice volumes from the Last Glacial Maximum to the Holocene. *Proceedings of the National Academy of Sciences*, *111*(43), 15296–15303. Retrieved from http://www.pnas.org/cgi/doi/10.1073/pnas.1411762111 doi: 10.1073/pnas.1411762111

Lliboutry, L. A. (1979). A critical review of analytical approximate solutions for steady state velocities and temperature in cold ice sheets. *Gletscherkd. Glazialgeol*, *15*(2), 135–148.

Martín, C., & Gudmundsson, G. H. (2012, oct). Effects of nonlinear rheology, temperature and anisotropy on the relationship between age and depth at ice divides. *The Cryosphere*, *6*(5), 1221–1229. Retrieved from https://www.the-cryosphere.net/6/1221/2012/ doi: 10.5194/tc-6-1221-2012

Martín, C., Hindmarsh, R. C. A., & Navarro, F. J. (2006). Dating ice flow change near the flow divide at Roosevelt Island, Antarctica, by using a thermomechanical model to predict radar stratigraphy. *Journal of Geophysical Research*, *111*(F1), F01011. Retrieved from http://doi.wiley.com/10.1029/2005JF000326 doi: 10.1029/2005JF000326

Martín, C., Hindmarsh, R. C. A., & Navarro, F. J. (2009, apr). On the effects of divide migration, along-ridge flow, and basal sliding on isochrones near an ice divide. *Journal of Geophysical Research*, *114*(F2), F02006. Retrieved from http://doi.wiley.com/10.1029/2008JF001025 doi: 10.1029/2008JF001025

Matsuoka, K., Hindmarsh, R. C., Moholdt, G., Bentley, M. J., Pritchard, H. D., Brown, J., ... Whitehouse, P. L. (2015, nov). Antarctic ice rises and rumples: Their properties and significance for ice-sheet dynamics and evolution. *Earth-*

Science Reviews, *150*, 724–745. Retrieved from http://dx.doi.org/10.1016/j.earscirev.2015.09.004https://linkinghub.elsevier.com/retrieve/pii/S0012825215300416 doi: 10.1016/j.earscirev.2015.09.004

Raymond, C. F. (1983, jan). Deformation in the Vicinity of Ice Divides. *Journal of Glaciology*, *29*(103), 357–373. Retrieved from https://www.cambridge.org/core/product/identifier/S0022143000030288/type/journal{_}article doi: 10.1017/S0022143000030288

Rignot, E., Mouginot, J., & Scheuch, B. (2017). MEaSUREs InSAR-Based Antarctica Ice Velocity Map, Version 2. *NASA National Snow and Ice Data Center Distributed Active Archive Center*. doi: 10.5067/D7GK8F5J8M8R

Rignot, E., Mouginot, J., & Scheuchl, B. (2011, sep). Ice Flow of the Antarctic Ice Sheet. *Science*, *333*(6048), 1427–1430. Retrieved from http://www.sciencemag.org/cgi/doi/10.1126/science.1208336 doi: 10.1126/science.1208336

Rudmin, J. W. (2010). Calculating the Exact Pooled Variance. *arXiv preprint arXiv:1007.1012*, 1–4.

Schytt, V. (1958). *Snow studies at Maudheim / Snow studies inland, The inner structure of the ice shelf at Maudheim as shown by core drilling. Schytt, Valter and 1949-1952, Norsk-britisk-svenske vitenskapelige ekspedisjon til Antartkis.* Oslo: Norsk Polarinstitutt,. Retrieved from https://trove.nla.gov.au/version/15459232

Siegert, M., Ross, N., Corr, H., Kingslake, J., & Hindmarsh, R. (2013, oct). Late Holocene ice-flow reconfiguration in the Weddell Sea sector of West Antarctica. *Quaternary Science Reviews*, *78*, 98–107. Retrieved from https://linkinghub.elsevier.com/retrieve/pii/S0277379113003028 doi: 10.1016/j.quascirev.2013.08.003

Still, H., Campbell, A., & Hulbe, C. (2019, apr). Mechanical analysis of pinning points in the Ross Ice Shelf, Antarctica. *Annals of Glaciology*, *60*(78), 32–41. Retrieved from https://www.cambridge.org/core/product/identifier/S0260305518000319/type/journal{_}article doi: 10.1017/aog.2018.31

Timmermann, R., & Goeller, S. (2017, sep). Response to Filchner–Ronne Ice Shelf cavity warming in a coupled ocean–ice sheet model – Part 1: The ocean perspective. *Ocean Science*, *13*(5), 765–776. Retrieved from https://www.ocean-sci.net/13/765/2017/ doi: 10.5194/os-13-765-2017

Van Liefferinge, B., & Pattyn, F. (2013, oct). Using ice-flow models to evaluate potential sites of million year-old ice in Antarctica. *Climate of the Past*, *9*(5), 2335–2345. Retrieved from https://www.clim-past.net/9/2335/2013/ doi: 10.5194/cp-9-2335-2013

van den Broeke, M. R. (2008). Depth and Density of the Antarctic Firn Layer Depth and Density of the Antarctic Firn Layer. *Arctic, Antarctic, and Alpine Research*, *40*(2), 432–438. doi: 10.1657/1523-0430(07-021)[BROEKE]2.0.CO;2

van der Veen, C. (1998, jun). Fracture mechanics approach to penetration of bottom crevasses on glaciers. *Cold Regions Science and Technology*, *27*(3), 213–223. Retrieved from http://linkinghub.elsevier.com/retrieve/pii/S0165232X98000068 doi: 10.1016/S0165-232X(98)00006-8

van Wessem, J. M., van de Berg, W. J., Noël, B. P. Y., van Meijgaard, E., Amory, C., Birnbaum, G., ... van den Broeke, M. R. (2018, apr). Modelling the climate and surface mass balance of polar ice sheets using RACMO2 – Part 2: Antarctica (1979–2016). *The Cryosphere*, *12*(4), 1479–1498. Retrieved from https://www.the-cryosphere-discuss.net/tc-2017-202/https://www.the-cryosphere.net/12/1479/2018/ doi: 10.5194/tc-12-1479-2018

Wearing, M. G. (2016). The Flow Dynamics and Buttressing of Ice Shelves. *PhD thesis, University of Cambridge*.

Wearing, M. G., Hindmarsh, R. C., & Worster, M. G. (2015, jul). Assessment

of ice flow dynamics in the zone close to the calving front of Antarctic ice shelves. *Journal of Glaciology*, *61*(230), 1194–1206. Retrieved from https://www.cambridge.org/core/product/identifier/S0022143000200361/type/journal{_}article doi: 10.3189/2015JoG15J116

Whitehouse, P. L., Bentley, M. J., Milne, G. A., King, M. A., & Thomas, I. D. (2012, sep). A new glacial isostatic adjustment model for Antarctica: calibrated and tested using observations of relative sea-level change and present-day uplift rates. *Geophysical Journal International*, *190*(3), 1464–1482. Retrieved from https://academic.oup.com/gji/article-lookup/doi/10.1111/j.1365-246X.2012.05557.x doi: 10.1111/j.1365-246X.2012.05557.x

Winter, K., Woodward, J., Ross, N., Dunning, S. A., Bingham, R. G., Corr, H. F. J., & Siegert, M. J. (2015, sep). Airborne radar evidence for tributary flow switching in Institute Ice Stream, West Antarctica: Implications for ice sheet configuration and dynamics. *Journal of Geophysical Research: Earth Surface*, *120*(9), 1611–1625. Retrieved from http://doi.wiley.com/10.1002/2015JF003518 doi: 10.1002/2015JF003518

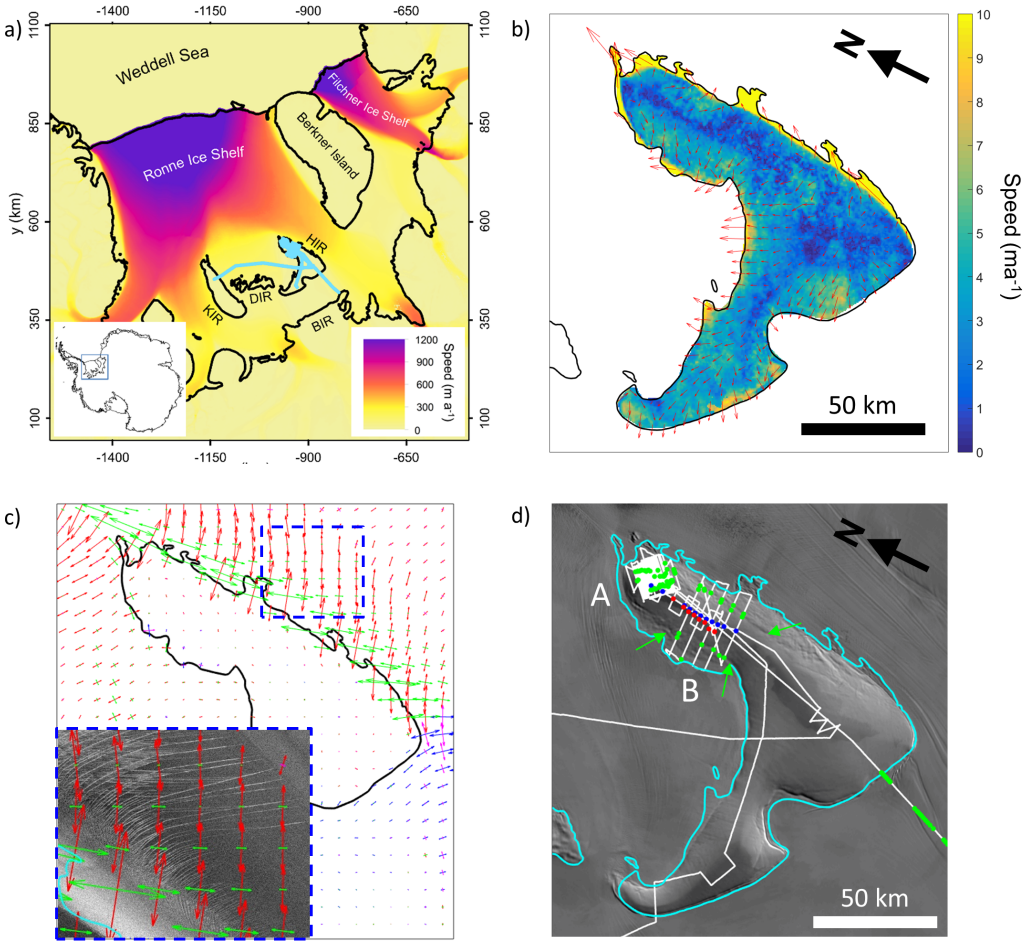

Figure 1. (a) Location and ice-surface speed (Rignot et al., 2011, 2017) map for Henry Ice Rise (HIR), Doake Ice Rumples (DIR), Korff Ice Rise (KIR) and Bungenstock Ice Rise (BIR) in the Weddell Sea sector of West Antarctica, as identified in the lower left inset. Pale blue lines show extent of ground-based ice-penetrating radar survey. Coordinates are given in WGS 84 / Antarctic Polar Stereographic, with origin at the South Pole. (b), (c) & (d) HIR: (b) Ice-surface speed with velocity vectors (red) (Rignot et al., 2017); (c) Principal Axes of Strain (PAS) (Wearing, 2016) (red - positive 1st PAS, blue - negative 1st PAS, magenta - positive 2nd PAS, green - negative 2nd PAS), insert shows alignment of PAS with surface crevasses observed from RAMP radar backscatter data (Jezek et al., 2013); (d) MODIS image (Haran et al., 2005) with extent of radar survey (white); closely spaced lines (250 - 500 m) labelled A, lines traversing ice divide labelled B. Ice divide (blue dots), low-amplitude arches (red dots), intersection of isochrones and the ice-base reflector (green dots) and elongated surface features (green arrows). The grounding line (Depoorter et al., 2013) is marked in each subfigure (black and cyan).

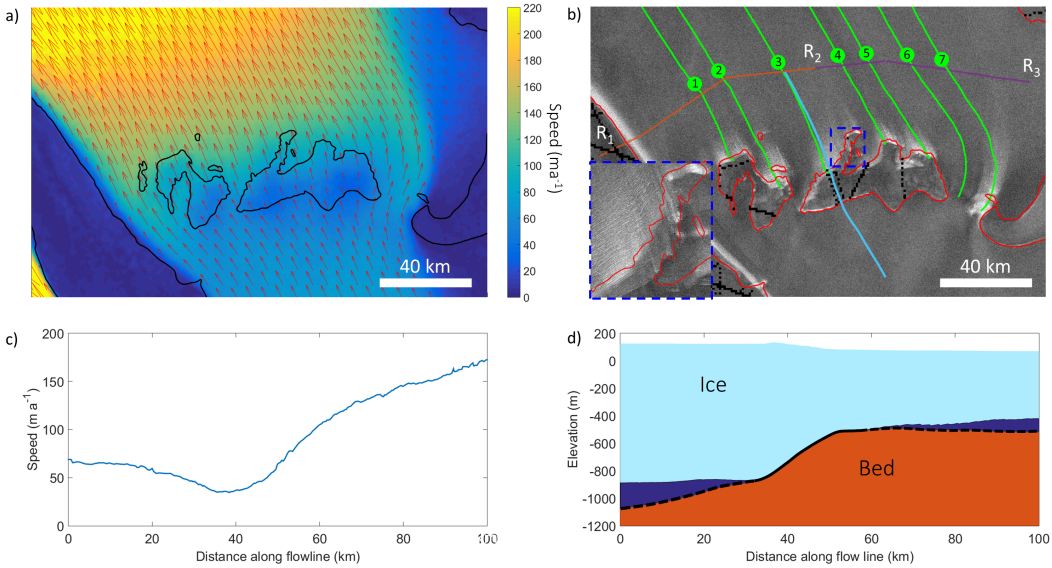

Figure 2. Doake Ice Rumples: (a) Ice-surface speed with velocity vectors (red) (Rignot et al., 2017). (b) RAMP radar backscatter image (Jezek et al., 2013) with; location of radar line downstream of DIR (R_1-R_2-R_3), transect flowline traversing rumples (blue), flowlines from downstream GL of DIR to radar profile (green, 1–7: West to East) and black squares indicating data coverage used in Bedmap2 (Fretwell et al., 2013). Insert shows zoomed-in view of surface crevassing. (c) Ice-surface speed traversing DIR along transect flowline. (d) Ice thickness and bedrock bathymetry along transect flowline; known bathymetry from Bedmap2 data coverage marked with solid black curve, dashed curve shows inferred bathymetry (Fretwell et al., 2013).

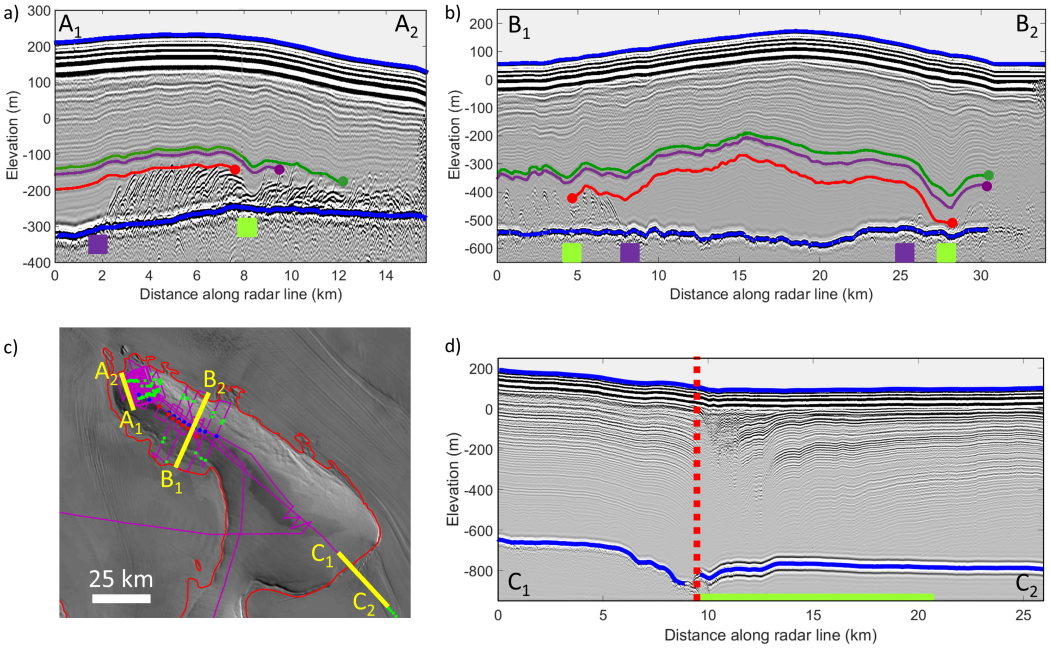

Figure 3. Radar profiles typical for each region of HIR. (a) A_1-A_2: over the northern promontory aligned approximately North-South. (b) B_1-B_2: profile traversing ice divide from West to East Flank. (c) MODIS image (Haran et al., 2005) with location of radar profiles. (d) C_1-C_2: profile traversing southern GL; the location of the GL is shown by the vertical dashed line. In all profiles both the surface and bed are highlighted (blue). For profiles A_1-A_2 and B_1-B_2 isochrones capping sets of relic basal crevasses are highlighted in red, purple and green, with relic-crevasse intercepts marked with a circle. (The full extent of these can be seen in Figure 4.) The locations of synclines are denoted with green squares and the minimum extent of isochrones intersecting the base of the ice shelf in profile C_1-C_2 is identified with a green line.

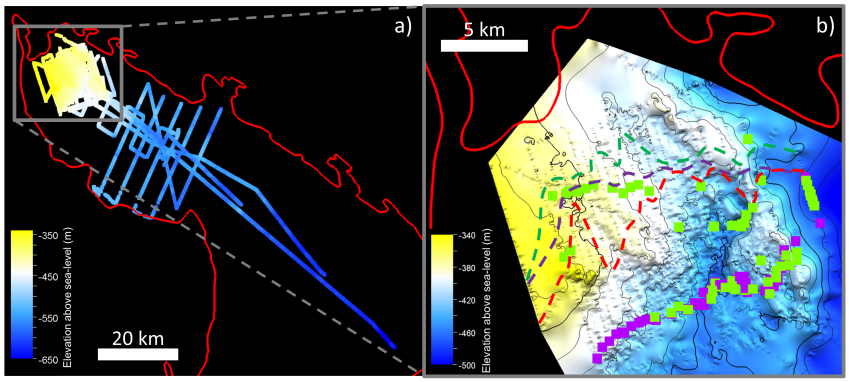

Figure 4. (a) Elevation of bed underlying HIR along radar lines. (b) Interpolated bathymetry over northern promontory, where radar lines are closely spaced. Ice flow is approximately from bottom-right to top-left. The upstream bound of buried relic crevasses is marked with purple squares. Dashed curves denote the locations of the intersection between capping isochrones and relic basal crevasses (deepest – red, shallowest – green) corresponding to isochrones picked in Figure 3. Synclines indicative of melt at former GLs are represented by green squares.

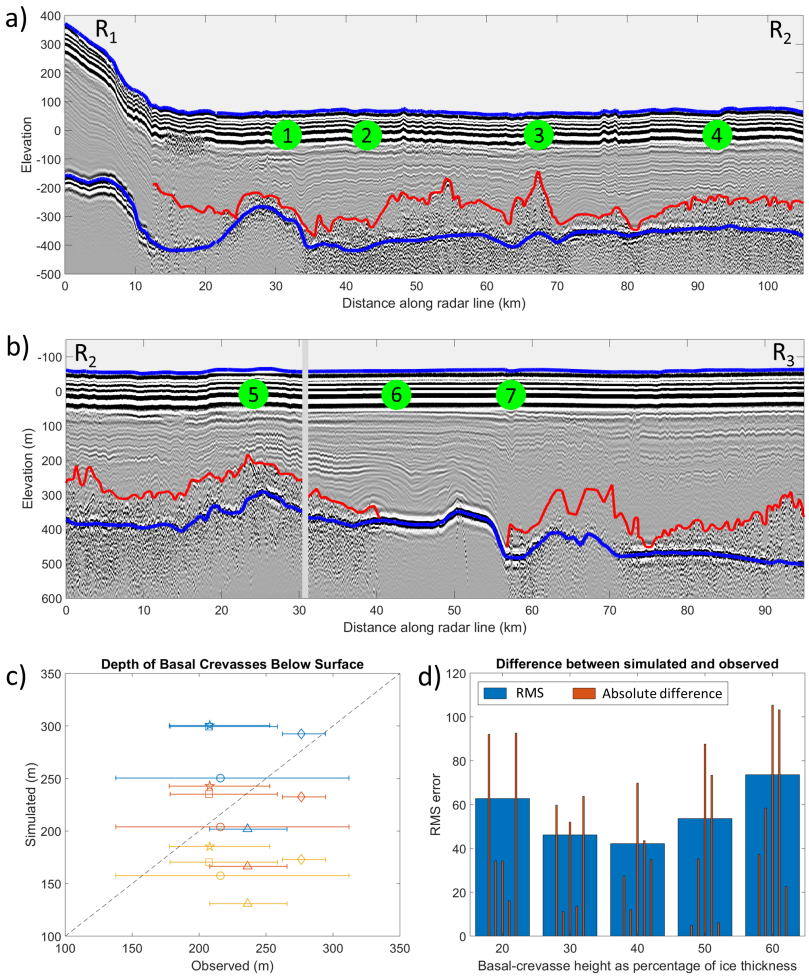

Figure 5. (a) and (b) Radar profile downstream of DIR, from KIR in the West (R_1) to HIR in the East (R_3). The location of this radar line can be seen in Figure 2b. The ice surface and base are highlighted (blue) along with the upper boundary of relic crevasses (red). The intersections of flowlines from DIR and the radar line are marked and correspond to the flowlines in Figure 2b. The vertical grey bar marks a data gap. (c) Plot of observed versus simulated ice thickness overlying basal crevasses for flowlines 1–5 that originate from DIR, using a range of initial basal crevasse heights as a percentage of ice thickness; 20% - blue, 40% - orange, 60% - yellow. Symbols denote different flowlines, with horizontal error bars indicating the range of depths within 2 km of the radar-flowline intersection along radar profile. (d) Root mean square (RMS) error for five different initial basal crevasse heights (blue bars), with absolute difference for each flowline (1–5) (red).

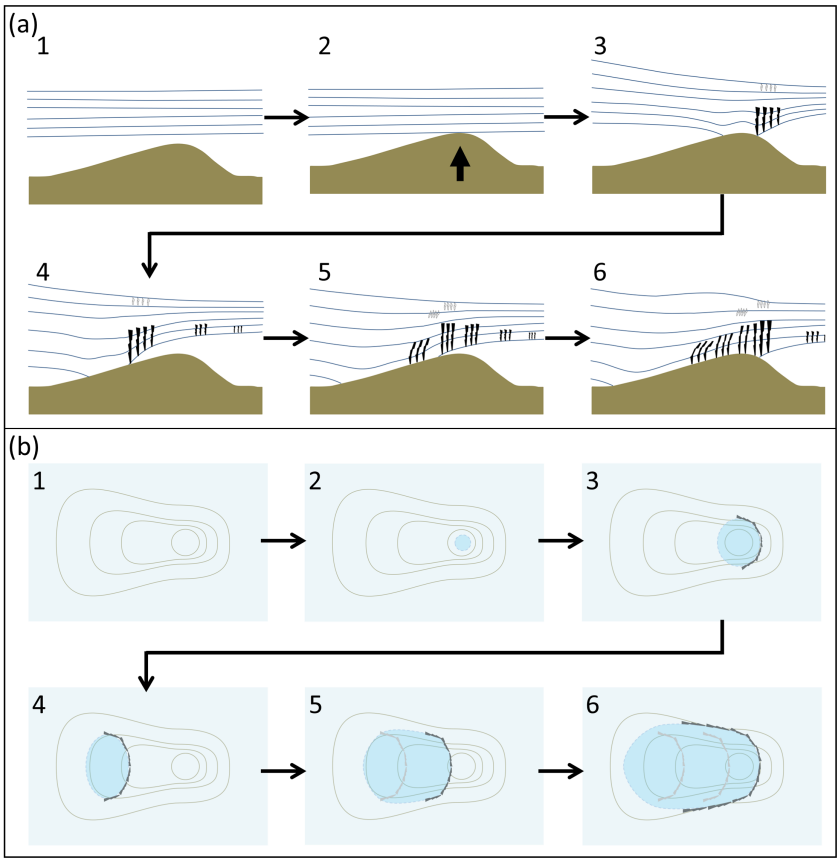

Figure 6. Conceptual model for the formation of HIR: (a) side view, (b) plan view. Stages: (1) floating ice shelf; (2) bathymetric high makes contact with ice shelf; (3) grounded on high point: compression and thickening upstream; extension and thinning downstream, with surface and basal crevasse formation; (4) ice rumple migrates upstream into deeper bathymetry (resembles DIR); (5) downstream GL advances, basal crevasses are grounded; (6) grounding over bathymetric high, buried crevasses become tilted (HIR today).

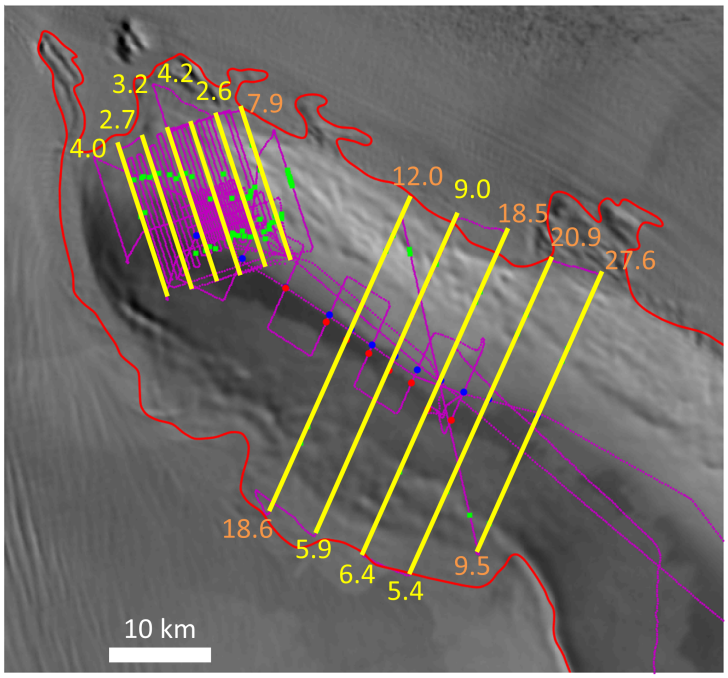

Figure 7. Dating estimates for the most upstream relic crevasse on each dated radar profile. Ages are given in kyr, with orange ages signifying that the presence of melt synclines has significantly affected age estimates. For full transect age estimates see SM Figures 2 and 7.

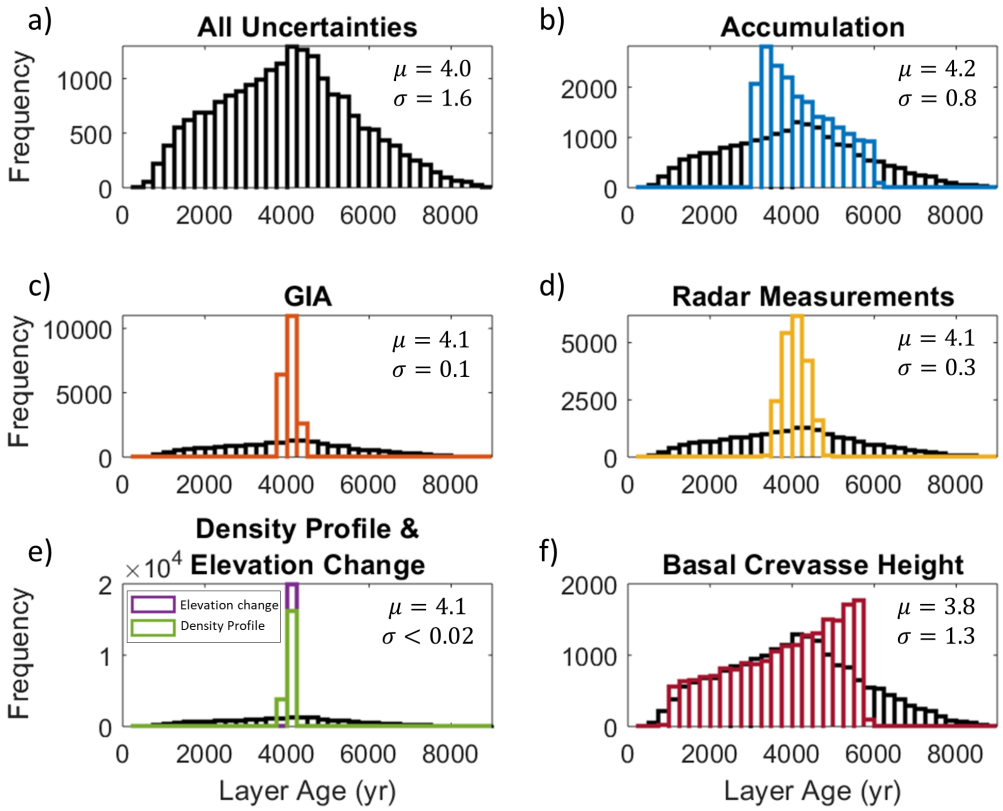

Figure 8. Histograms showing the frequency distribution of age estimates when the uncertainty in each model parameter is included in the Monte-Carlo procedure, for the onset of crevassing on radar line A_1 - A_2. (a) All uncertainties are included, with this distribution included in all other plots for comparison. (b) Uncertainty in accumulation rate only. (c) Uncertainty in GIA rate. (d) Uncertainties from radar measurements (surface elevation, relic-crevasse and bed depth). (e) Uncertainties in vertical density profile (surface density and densification rate) (green) and surface elevation change (purple). (f) Uncertainty in basal crevasse height. Table 1 provides the ranges over which each parameter is varied.